# Size- and Composition-Dependent Radio Frequency Magnetic Permeability of Iron Oxide Nanocrystals

Hongseok Yun,[†] Xiyu Liu,[‡] Taejong Paik,[†] Duraivelan Palanisamy,[‡] Jungkwun Kim,[§] William D. Vogel,[‖] Arthur J. Viescas,[‖] Jun Chen,[‡,#] Georgia C. Papaefthymiou,[‖] James M. Kikkawa,[⊥] Mark G. Allen,[§] and Christopher B. Murray*,[†,‡]

[†]Department of Chemistry, [‡]Department of Materials Science and Engineering, [§]Department of Electrical and Systems Engineering, and [⊥]Department of Physics and Astronomy, University of Pennsylvania, Philadelphia, Pennsylvania 19104, United States, and [‖]Department of Physics, Villanova University, Villanova, Pennsylvania 19085, United States. [#]Present address: HGST, a Western Digital company, 3403 Yerba Buena Road, San Jose, California 95135, United States.

ABSTRACT We investigate the size- and composition-dependent ac magnetic permeability of superparamagnetic iron oxide nanocrystals for radio frequency (RF) applications. The nanocrystals are obtained through high-temperature decomposition synthesis, and their stoichiometry is determined by Mössbauer spectroscopy. Two sets of oxides are studied: (a) as-synthesized magnetite-rich and (b) aged maghemite nanocrystals. All nanocrystalline samples are confirmed to be in the superparamagnetic state at room temperature by SQUID magnetometry. Through the one-turn inductor method, the ac magnetic properties of the nanocrystalline oxides are characterized. In magnetite-rich iron oxide nanocrystals, size-dependent magnetic permeability is not observed, while maghemite iron oxide nanocrystals show clear size dependence. The inductance, resistance, and quality factor of hand-wound inductors with a superparamagnetic composite core are measured. The superparamagnetic nanocrystals are successfully embedded into hand-wound inductors to function as inductor cores.
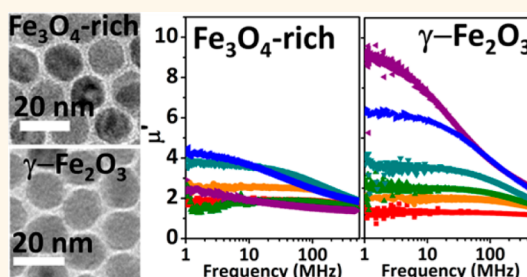
KEYWORDS: magnetite · maghemite · superparamagnetism · radio frequency · magnetic susceptibility · inductor

Magnetic nanocrystals (NCs) have been widely used for applications such as dc[1−3] and ac[4−6] electromagnetic devices, medical diagnostics,[7−9] clinical therapy,[10−12] and stealth technology.[13−15] Among the various ac applications, the use of nanocrystalline magnetic materials in the design of inductors[16−18] and transformers[19−21] is of particular interest due to the desire to reduce the volume of magnetic components for the miniaturization of electromagnetic devices. Incorporating the magnetic colloidal NCs offers the potential for low-cost and rapid fabrication of the miniaturized devices *via* simple solution-based deposition and infiltration.[22−25] In addition, the properties of magnetic NCs are tunable with precisely controlled size, shape, and composition,[26−29] which provides a new scope to improving the performance of electromagnetic devices.

In order to utilize magnetic NCs in miniaturized magnetic components, achieving high operating frequencies while benefiting from the high permeability of magnetic core material is critical.[30−34] However, magnetic materials under high-frequency field suffer from low ferromagnetic resonance frequency, hysteresis loss, and eddy current loss. Ferromagnetic resonance occurs when the frequency of an external ac magnetic field coincides with the precession frequency of the magnetization vector around the anisotropy field in the ferromagnetic material.[35] At the resonance frequency, magnetic energy is absorbed and subsequently dissipated as heat. Simultaneously, the magnetization relaxes back to its original magnetization direction and precession mode. Hysteresis loss is energy wasted in repeatedly reversing the magnetization direction of ferromagnetic materials under an ac field.[35] Microscopically, this loss comes from the energy required for field activation over domain wall pinning sites and the subsequent loss of this energy to the lattice

after field activation completes.[36,37] Eddy current loss is the resistive power dissipation from the induced current inside a conductive material.[35,38] These effects limit the operation of radio frequency (RF) electromagnetic devices with conventional magnetic cores such as Permalloy, Supermalloy, nickel zinc ferrite, and manganese zinc ferrite.[35,39,40]

Superparamagnetic NCs are good candidates for low-loss RF magnetic materials. Superparamagnetic behavior is expressed in single-domain magnetic nanoparticles due to thermally induced magnetic reorientation above the blocking temperature. The Néel relaxation time of superparamagnetic NCs is expressed in the Néel−Arrhenius equation, $\tau_N = \tau_0 \exp(E_a/(k_B T))$, where the physical parameters of NCs are defined as follows: $1/\tau_0$ is attempt frequency for magnetization reversal, E_a is the anisotropy barrier for the particle, which, in the absence of interparticle interactions, is taken to be KV where K is the magnetic anisotropy energy density and V is the volume of the NC. Thermally assisted magnetization reversals can take place and the nanoparticles exhibit superparamagnetic behavior above a characteristic blocking temperature, T_b, with zero coercity.[41−43] Therefore, the superparamagnetic behavior of NCs can effectively suppress hysteresis loss at high frequencies. Since the NCs are surrounded by an insulating organic ligand shell, rendering the nanocrystal ensemble nonconductive, eddy current loss is also suppressed/eliminated. Recently, Kura et al. reported size-dependent high-frequency dynamics of Fe NCs,[6] and Song et al. reported an increased cutoff frequency for Fe3O4 NCs after coating the iron cores with SiO2 shells.[5] These results show that the ferromagnetic resonance frequency of superparamagnetic NCs can be pushed to more than 1 GHz, which is of great advantage to extend the use of magnetic NCs to RF devices. Further investigation is still necessary on how the size, shape, crystalline structure, and chemical composition of NCs affect their magnetic permeability at RF frequencies in order to design NC-based ac devices with optimized RF magnetic properties. In addition, understanding RF properties of magnetic NCs is important to their use not only in low-energy-loss applications but also in high-energy-loss desired applications such as hyperthermia cancer treatment, which needs to *maximize* losses to enhance the thermal energy release from nanocrystals.[12,26,44,45]

So far, numerous studies have investigated the dc magnetic properties of nearly monodisperse NCs such as iron oxide,[46] ferrites,[26,27,29] cobalt,[28] nickel,[47,48] and FePt.[3] However, even though there has been much effort to utilize magnetic nanocomposites in ac applications such as inductor cores[5,6,16] and hyperthermia cancer treatment,[12,26,44,45] frequency-dependent magnetic properties at radio frequencies of magnetic NCs as a function of size, shape, and composition have not

been fully understood. In the case of iron oxide NCs, which are the most widely used magnetic NCs, it has been reported that the stoichiometry of as-synthesized iron oxide NCs changes from magnetite (Fe_3O_4) rich to maghemite (γ-Fe_2O_3) rich structure upon oxidation.[49] It is well known that this oxidation severely affects the dc magnetic properties,[50] but concomitant changes in ac magnetic properties under RF field have not been extensively studied.

In this report, superparamagnetic iron oxide NCs are systematically examined to understand the particle size and composition dependence of magnetic permeability. As-synthesized and naturally oxidized iron oxide NCs, oxidized under ambient condition, are compared to clarify the composition or stoichiometry dependence of magnetic permeability and the environmental stability of iron oxide NCs. For both sets of NCs, structural stoichiometry and electronic and magnetic characteristics are analyzed using Mössbauer spectroscopy, dc magnetization measurements *via* superconducting quantum interference device (SQUID) magnetometry, and ac magnetic characterization by using a one-turn inductor model with an Agilent 4395A impedance analyzer and a 16454A magnetic material test fixture. Finally, the ac characterization of inductors with iron oxide NC cores is conducted.

RESULTS AND DISCUSSION

Iron oxide NCs are prepared by modifying methods previously reported by Hyeon et al.[46,51] Highly uniform NCs with various sizes are synthesized, and the size is increased by increasing the amount of oleic acid added. In Figure 1 are the TEM images of as-synthesized iron oxide NCs (Figure 1a−f) and aged iron oxide NCs (Figure 1h−m). In order to precisely analyze the size-dependent properties, it is essential to determine the size and size distribution of NCs by bulk-based measurement, collecting ensemble average structural information, which are presented in Figure 1g (as-synthesized samples) and 1n (aged samples). The NCs exhibit good monodispersity with the size deviation from 7% to 9% based on SAXS fitting and from 5% to 8% based on the TEM images (Figures S1 and S2). All the NC sizes referred to in this report are the values calculated by SAXS fitting. The average size of NCs is determined by SAXS measurement with the experimental data fitted to the standard spherical model weighted by lognormal distribution, which are presented as black curves in the SAXS data. The size ranges are from 10.2 to 19.7 nm of as-synthesized iron oxide NCs and from 8.6 to 17.0 nm of aged iron oxide NCs. Iron oxide NCs in this size range are selected for study because NCs in this range (a) show superparamagnetic behavior and (b) can be easily dispersed in volatile solvents, which has a potential to be used in solution-based deposition processes.
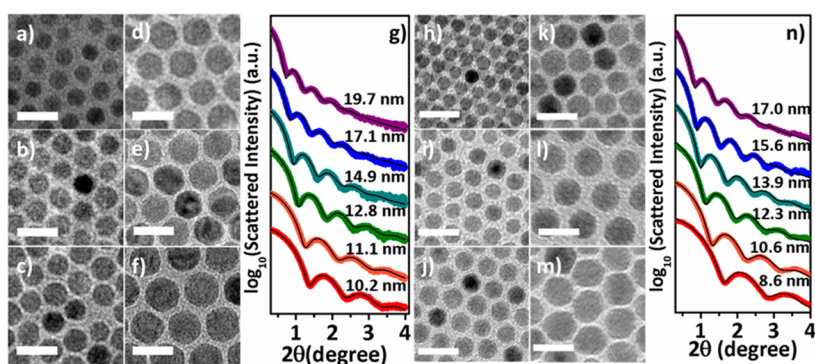
Figure 1. Set of images on the left half represent the TEM images of (a) 10.2 nm, (b) 11.1 nm, (c) 12.8 nm, (d) 14.9 nm, (e) 17.1 nm, and (f) 19.7 nm as-synthesized iron oxide NCs and (g) their small-angle X-ray scattering data. The set of images on the right half represent the TEM images of (h) 8.6 nm, (i) 10.6 nm, (j) 12.3 nm, (k) 13.9 nm, (l) 15.6 nm, and (m) 17.0 nm aged iron oxide NCs and (n) their small-angle X-ray scattering data. All the scale bars represent 20 nm. The black lines in the SAXS data represent the simulated fits for each size of the NCs.

Polymorphs of iron oxide crystal structures include magnetite (Fe_3O_4), maghemite (γ-Fe_2O_3), hematite (α-Fe_2O_3), and wüstite ($Fe_{1-x}O$). Although the composition of iron oxide synthesized from iron-oleate precursors is known to be primarily a mixture of magnetite and maghemite,[46] magnetite can be further oxidized under air to form maghemite structures.[49] In the magnetite structure, all of the ferrous ions and half of the ferric ions are found in octahedral [B] sites. The other half of ferric ions are found in tetrahedral (A) sites. This is known as the inverse spinel structure. As oxidation proceeds, ferrous ions diffuse outwardly from the interior of the iron oxide NCs toward the surface of the particle, while the particle keeps its morphology and crystal structure.[49] The oxidation of ferrous ions reduces both the saturation magnetization and magnetic anisotropy of the iron oxide NCs, which in turn can alter their ac magnetic behavior.[50,52] Therefore, it is important to determine the degree of ferrous iron oxidation in the magnetite structure of our iron oxide NCs.

As it is difficult to distinguish magnetite NCs from maghemite NCs with X-ray diffraction due to their crystal structural resemblance (Figure S3), we use Mössbauer spectroscopy to probe the electronic structure of the iron ions in order to determine their oxidation state and thus derive the stoichiometry of our as-synthesized (magnetite-rich) and aged (maghemite) NCs. Representative data are shown in Figure 2. The black solid line through the experimental points is a least-square fit to a superposition of theoretical spectra shown in colored solid lines corresponding to different iron subsites in the structure. The left half of Figure 2 shows the Mössbauer spectra of (a) 17.0 nm and (b) 10.6 nm maghemite nanocrystals at 300 and 4.2 K, while the right half shows the corresponding spectra for (c) 19.7 nm and (d) 10.2 nm magnetite-rich NCs. The selected sizes presented correspond to relatively large and small particles studied. At 4.2 K, sharp magnetically split spectra are observed in all cases, indicating blocked particle magnetic moments with a relaxation

time $\tau_N > \tau_L$, where $\tau_L \approx 10$ ns is the Larmor precession time of the iron excited state nuclear spin in the internal magnetic field of the particle.[53] As described below, spectral analysis of these blocked (slow relaxation) magnetic spectra permits the estimation of the degree of iron oxidation in the spinel crystallographic structure, (i.e., stoichiometry) of the samples. At 300 K the spectra of the larger NCs (17.0 nm maghemite and 19.7 nm magnetite-rich) sit on a broad, absorption envelope due to the presence of intermediate relaxation (IR) effects ($\tau_N \approx \tau_L$). In contrast, the spectra of the smaller NCs (10.6 nm maghemite and 10.2 nm magnetite-rich) exhibit motional narrowing due to fast relaxation effects ($\tau < \tau_L$) at 300 K.

At 4.2 K spectra of maghemite samples are fit to superpositions of iron subsites corresponding to tetrahedral (A) (spectral component in blue) and octahedral [B] (spectral component in purple) iron sites.[54] Parameters derived from spectral fitting are tabulated in Table 1. These spectral signatures are consistent with the presence of γ-Fe_2O_3 nanocrystals. At 300 K an additional broadened absorption envelope (in cyan) is superimposed, which arises from a complex interplay between thermally driven collective magnetic excitations[55] of the magnetization about the anisotropy axes of the particles and interparticle interactions.[56] The latter are stronger in samples containing larger particles, due to their larger net moments, whereas the former are enhanced in smaller sized particles. Magnetic dipole−dipole interactions between particles prevent the NC assemblies from fully entering the superparamagnetic regime within the characteristic measuring time of the Mössbauer technique of $\tau_{M\ddot{o}ss} = 10$ ns, which is 8 to 9 orders of magnitude shorter than that of SQUID magnetometry, where $\tau_{SQUID} = 1$ to 100 s. This results in the broad absorption envelopes observed that are characteristic of intermediate relaxation effects (simulated by the broadened spectral components in cyan) at room temperature. For the smaller maghemite particles in Figure 2, interparticle
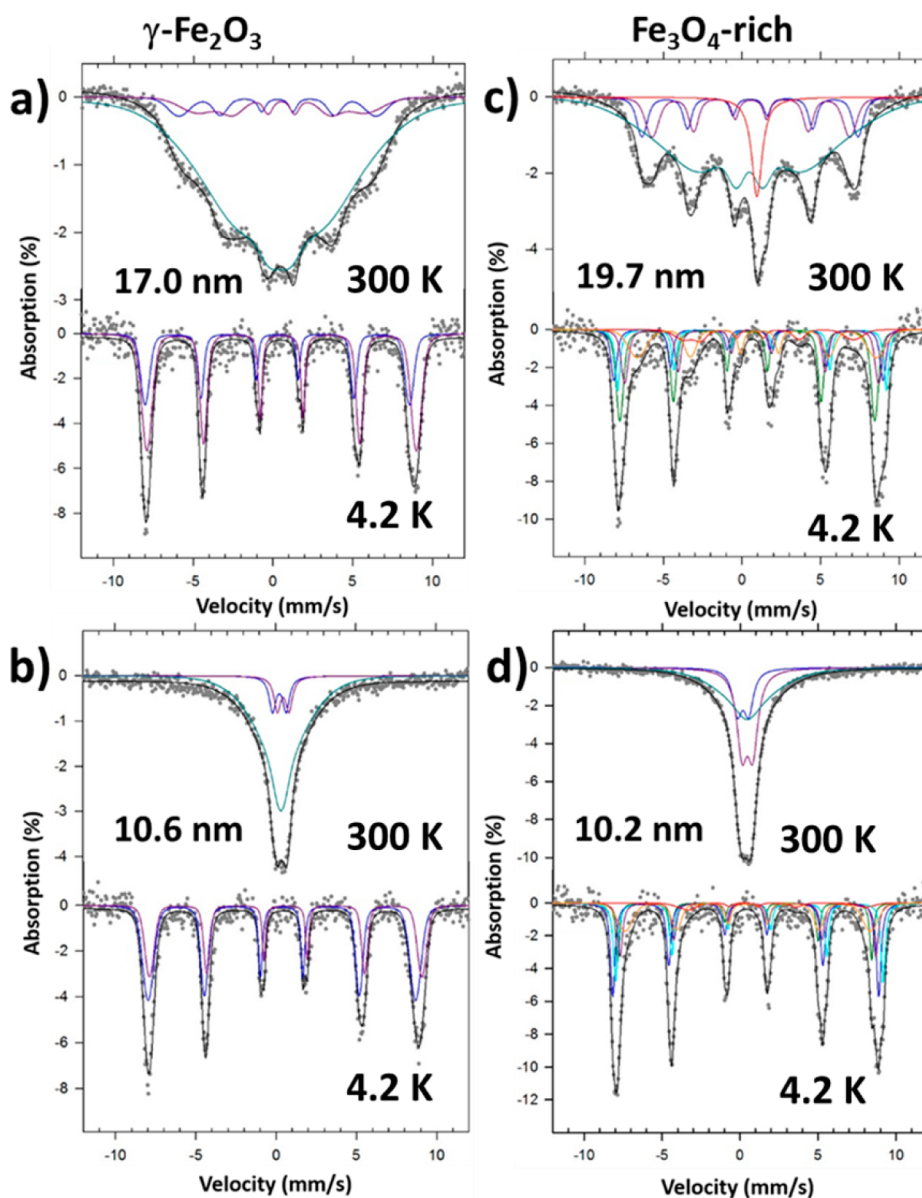
Figure 2. Mössbauer spectra of selected NC samples. Left side: maghemite NCs at 300 and 4.2 K (a) 17.0 nm, (b) 10.6 nm. Right side: magnetite-rich NCs at 300 and 4.2 K (c) 19.7 nm, (d) 10.2 nm. The experimental points are least-squares fitted (black line) to a superposition of theoretical spectra of tetrahedral (A) (blue) and octahedral [B] (purple) sites, intermediate relaxation (IR) components (cyan), and interfacial $Fe_{1-x}O/Fe_3O_4$ phases (red) (see text and Table 1).

interactions are weakened due to their smaller net moments, leading to motional narrowing and collapse of the magnetic spectral signature at room temperature as the particles increasingly enter the superparamagnetic regime. That is, at room temperature the spectra of the 17.0 nm maghemite NCs are dominated by intermediate relaxation effects due to stronger interparticle interactions, while those of the 10.6 nm NCs are dominated by fast relaxation effects, producing largely collapsed, paramagnetic doublets indicating mostly superparamagnetic (noninteracting) particles at the Mössbauer time scale.

In the case of magnetite-rich NCs, the situation is further complicated by the well-known Verwey transition,[57] which is a first-order metal−insulator transition,

originating from a slight distortion in the crystal structure from inverse cubic spinel to monoclinic, occurring at $T_V = 120$ K in the bulk. The low-temperature monoclinic form has discrete iron valence states producing sharp absorption spectra. Above T_V fast electron hopping takes place between the Fe^{2+} and Fe^{3+} ions in octahedral [B] sites, resulting in pairwise electronic delocalization. This drastically changes the Mössbauer spectral features to the superposition of two magnetic components corresponding to $Fe^{2.5+}$ in [B] sites (simulated in purple) and Fe^{3+} in (A) sites (simulated in blue) at RT.[58,59] Again in order to properly simulate these 300 K spectra, an additional, severely broadened absorption envelope had to be superimposed (simulated in cyan) corresponding to intermediate

TABLE 1. Mössbauer Hyperfine Parameters Derived from Spectral Fits: δ, Isomer Shift Relative to Metallic Iron at RT, ΔE_Q, Quadrupole Splitting, H_{hf}, Hyperfine Magnetic Field, (A) Tetrahedral Sites, [B] Octahedral Sites, IR, Intermediate Relaxation, Interfacial, $Fe_{1-x}O/Fe_3O_4$

sample	T (K)	site identification	δ (mm/s)	ΔE_Q (mm/s)	H_{hf} (T)	area (%)
γ-Fe$_2$O$_3$						
17.0 nm	300	Fe^{3+} (A)	0.25		38.2	7
		Fe^{3+} [B]	0.50		32.4	9
		IR	0.41			84
	4.2	Fe^{3+} (A)	0.32		51.3	50
		Fe^{3+} [B]	0.57		52.3	50
10.6 nm	300	Fe^{3+} (A)	0.25	0.85		10
		Fe^{3+} [B]	0.49	0.73		9
		IR	0.38			91
	4.2	Fe^{3+} (A)	0.35		51.5	62
		Fe^{3+} [B]	0.60		52.5	38
Fe$_3$O$_4$-rich						
19.7 nm	300	Fe^{3+} (A)	0.32		42.5	11
		$Fe^{2.5+}$ [B]	0.58		38.9	13
		IR	0.48			68
		interfacial*	0.95			8
	4.2	Fe^{3+} (A)	0.33		50.2	29
		Fe^{3+} [B]	0.41		53.0	13
		Fe^{3+} [B]	0.63		52.9	14
		Fe^{2+} [B]	1.02	−0.18	47.0	19
		Fe^{2+} [B]	1.10	1.19	33.4	7
		IR*	0.61		49.9	18
10.2 nm	300	Fe^{3+} (A)	0.19	0.72		18
		$Fe^{2.5+}$ [B]	0.46	0.70		37
		IR	0.46			45
	4.2	Fe^{3+} (A)	0.32		50.2	25
		Fe^{3+} [B]	0.34		52.7	30
		Fe^{3+} [B]	0.61		53.0	22
		Fe^{2+} [B]	1.20	1.95	36.3	5
		Fe^{2+} [B]	1.19		48.1	17
		IR	0.58		50.2	16

relaxation spectra. Additionally, the larger NCs of 19.7 nm diameter contain a small amount ($\sim$8%) of a paramagnetic iron component identified as wüstite ($Fe_{1-x}O$), indicated by the relatively sharp spectral feature in red in Figure 2c.[60,61] Wüstite contains only Fe^{2+}, is paramagnetic at room temperature, and undergoes a paramagnetic-to-antiferromagnetic phase transition at 200 K. It has been previously reported to coexist in large particles of magnetite as an interfacial $Fe_{1-x}O/Fe_3O_4$ phase.[62]

The degree of iron oxidation can be determined from the relative spectral areas of the different iron subcomponents, under the assumption that the recoil-free fraction[46] is similar for all iron sites. This assumption is more valid at low temperatures. Therefore, we have made use of the 4.2 K spectra to determine the stoichiometry of the magnetic component ascribed to Fe_3O_4 within the spectral decomposition of our NCs. For stoichiometric magnetite one expects an intensity ratio of ferrous to ferric iron of 1:2. Deviations from this value in our measured spectra are used to get an estimate of the degree of oxidation of our

magnetite-rich NCs.[63] However, our nanocrystals contain additional Fe^{2+} assigned to $Fe_{1-x}O$ or interfacial $Fe_{1-x}O$–Fe_3O_4 phases, which however remain largely unresolved at 4.2 K but contribute to the broad IR spectral absorption envelopes (Table 1). For the 19.7 nm magnetite-rich NCs we obtain Fe^{2+}/Fe^{3+} = 0.464, indicating a level of 7.2% oxidation. For the 10.2 nm nanoparticles this ratio has dramatically decreased to Fe^{2+}/Fe^{3+} = 0.285, indicating an oxidation level of 43%, which is similar to the degree of oxidation reported by Hyeon et al.: Fe^{2+}/Fe^{3+} = 0.285 in the case of 9 nm and Fe^{2+}/Fe^{3+} = 0.43 in the case of 16 nm particles.[46]

Figure 3 displays the dc magnetic characterization of iron oxide NCs. Blocking temperature (T_b), coercivity (H_c), and the ratio between remnant magnetization and saturation magnetization (M_r/M_s) at 15 K are summarized in Table 2. For zero field cooled (ZFC) measurements, the NCs are cooled from 300 K to 15 K without an external magnetic field. Then, a 0.01 T static magnetic field is applied and the magnetic moment of the sample is measured as the temperature returns to 300 K. T_b is determined at the maximum value of the normalized magnetic moment, M/M_{max}. This observed blocking temperature is dependent on the time scale of observation[64,65] and results from the combined effect of the magnetic anisotropy barrier, KV, of the isolated particle and the interparticle interactions, both of which become stronger with increasing particle size. For the larger NCs, we expect interparticle interactions to be sizable, producing a maximum in the magnetization of the ZFC curves at 200 K, which is best described as a spin-freezing temperature due to strong dipole–dipole interactions between particles, resulting in a spin-glass-like system within the granular assembly. The presence of strong interparticle interactions is evinced by (a) the shape of the ZFC/FC curves and (b) the values of M_r/M_s at 15 K, as we further elaborate below, as well as (c) the presence of the IR spectral features in the room-temperature Mössbauer spectra, as we have discussed above.

The severe flattening of the field-cooled (FC) curves at $T < T_b$ shown in Figures S4 and S5 is often interpreted as evidence for strong interparticle interactions.[66−68] However, since the spin-blocking temperature values of all the samples are below 300 K (Figure 3a and b, Table 2), they are confirmed to be in the superparamagnetic state at room or higher temperatures. Also, the hysteresis curves at 15 K (Figures 3c,d, S6, and S7) and 300 K (Figure S8) support the observation of the superparamagnetic state of NCs at room temperature. The hysteresis curves at 300 K show zero coercivity for all the samples, with size-dependent coercivity observed at 15 K for both sets of NCs. At 15 K, the as-synthesized magnetite-rich samples exhibit larger coercivities and slanted hysteresis loops compared to the maghemite samples. This is attributed to the
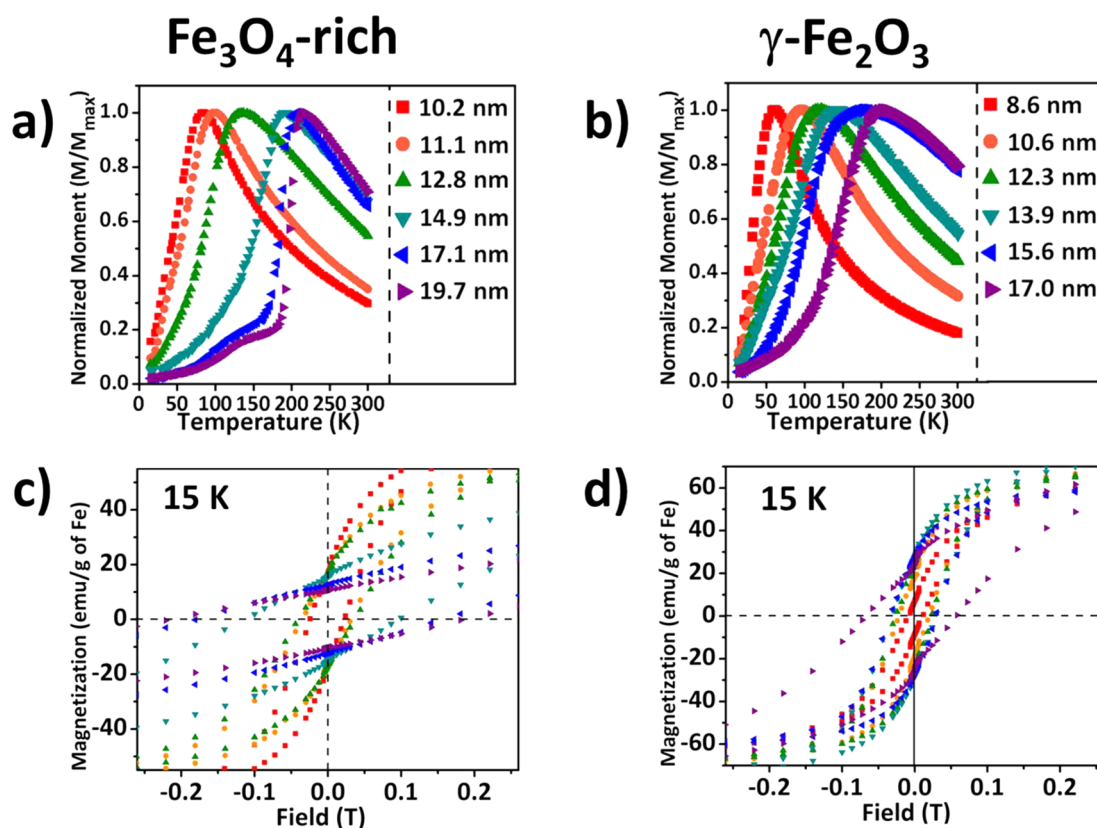
Fe₃O₄-rich

γ-Fe₂O₃

Figure 3. Zero-field cooling curves of (a) magnetite-rich iron oxide and (b) maghemite iron oxide samples of different sizes. Enlarged hysteresis curves of (c) magnetite-rich iron oxide NCs and (d) maghemite iron oxide NCs at 15 K. Full sweep (from 3 T to −3 T) hysteresis curves are presented in Figure S6 (magnetite-rich) and S7 (maghemite).

TABLE 2. Coercivity (H_c) Values at 15 K, Blocking Temperatures (T_b), and the Ratio between Remnant Magnetization (M_r) and Saturation Magnetization (M_s) of Iron Oxide NCs

	Fe₃O₄-rich				γ-Fe₂O₃		
size (nm)	H_c at 15 K (mT)	T_b (K)	M_r/M_s	size (nm)	H_c at 15 K (mT)	T_b (K)	M_r/M_s
10.2 ± 0.8	32	85.2	0.17	8.6 ± 0.7	12	62.1	0.09
11.1 ± 0.9	35	100.7	0.21	10.6 ± 0.8	20	98.3	0.22
12.8 ± 0.9	40	134.1	0.23	12.3 ± 1.0	24	120.8	0.31
14.9 ± 1.2	115	191.62	0.22	13.9 ± 1.0	33	142.4	0.29
17.1 ± 1.5	181	208.9	0.21	15.6 ± 1.2	33	174.4	0.37
19.7 ± 1.7	215	217.5	0.19	17.0 ± 1.5	58	203.1	0.24

presence of Fe^{2+} in the former and absence in the latter. In maghemite, the local ionic magnetic moment is due only to spin angular momentum, since the orbital angular momentum of the half-filled $3d^5$ electronic shell is usually quenched. In contrast, the sixth electron of Fe^{2+} in the magnetite-rich $3d^6$ structures can have unquenched orbital angular momentum,[69] which couples the magnetic moment of the particle to the lattice through the spin–orbit interaction, thus increasing the first magnetocrystalline anisotropy constant in magnetite ($K_1 \approx -1.1 \times 10^4$ J/m³)[70] compared to maghemite

($K_1 \approx 10^3$ J/m³).[71] In turn, this reduces the coercivity and produces steeper hysteresis loops in maghemite samples. However, in NCs, surface and strain effects add to the overall effective anisotropy that governs the observed coercvities.[72,73] In addition, differences in the strength of interparticle interactions also contribute.

For the magnetite-rich NCs, the overall shape of the ZFC magnetization curves of the larger NCs is qualitatively different than those of the smaller NCs. Specifically, the 17.1 and 19.7 nm magnetite-rich NCs have small initial slopes and exhibit a broad hump between 100 and 150 K, which is absent in the smaller magnetite-rich and in all maghemite nanocrystals. This hump may be partially attributed to the Verwey transition of magnetite, which is known to occur at 120 K in the bulk.[74] However, both small NC size and nonstoichiometry suppress T_V to lower temperatures[75,76] compared to that of the bulk. Anomalies in the magnetization of magnetite nanocrystals have been previously reported to occur above the Verwey transition temperature[77] and have been associated with the complex temperature dependence of the first magnetocrystalline anisotropy constant K_1 of magnetite.[78] Thus, the observed hump may be associated with the combined effect of this process and the Verwey transition. However, it may also reflect some spin reorientation transition within the particle ensemble. The steep

rise of the magnetization at around 200 K for the 19.7 and 17.1 nm magnetite-rich nanocrystals in Figure 3b is partially due to the presence of wüstite, $Fe_{1-x}O$, which is known to undergo a paramagnetic-to-antiferromagnetic phase transition at 200 K.[60]

The dynamic magnetic properties of NCs are usually examined through the real and imaginary components of the ac susceptibility and their dependence on the frequency of the applied alternating magnetic field. In the dense nanoparticulate samples used in this study to form a toroidal sample, the nanocrystals are not free to rotate. Below T_b, the reversal of the magnetization of the single-domain particle over the anisotropy energy barrier must take place through the Néel spin relaxation process. In a simple phenomenological model, interparticle interactions can be considered as a perturbation to the anisotropy barrier,[56] $E_a = (KV + E_{int})$, where E_{int} gives a measure of the strength of interparticle magnetic interactions.

The presence of interparticle interactions in our nanocrystal assemblies is witnessed by the low values of remanence-to-saturation ratio, M_r/M_s, observed in the hysteresis loops at 15 K in Figure 3. The magnetite-rich samples have $M_r/M_s \approx 0.2$ irrespective of NC size, while the maghemite samples exhibit some variation with values ranging between 0.09 and 0.37 (Table 2). It is well known that an assembly of noninteracting, randomly oriented, uniaxial magnetic particles have $M_r/M_s = 0.5$.[79] Thus, strong interparticle interactions appear to exist in our samples, which are also evinced in the Mössbauer spectra, which show strong intermediate relaxation envelopes persisting to RT. Moreover, these low values of remanence-to-saturation ratio reveal the existence of interactions that are overall antiferromagnetic in nature.[80,81]

The dynamic magnetic properties of nanoparticles are usually studied through ac magnetic susceptibility, χ, measurements. For blocked nanoparticles, the relaxation time enters the expressions for the frequency dependence of the real and imaginary parts of the magnetic susceptibility[82] according to equation SI (1) presented in the SI file. In order to determine the dynamic magnetic properties of our NCs at radio frequencies, we performed relative magnetic permeability measurements, $\mu_r = \mu/\mu_0 = 1 + \chi$, as they are more readily related to investigations of their use as inductors. These measurements were conducted using the one-turn inductor model.[83,84] In this method, a coaxial cable is considered as a one-turn inductor. The reactance and resistance of the one-turn inductor can be measured and converted into the real and imaginary parts of permeability. The relative permeability (μ_r) is written as eq 1.[83,84]

$$\mu_r = \frac{(Z_m - Z_{sm})}{jf\mu_0 h \ln\frac{c}{b}} + 1 \qquad (1)$$

Here Z_m is the impedance measured in the presence of the sample, Z_{sm} is the impedance without the sample, f is the frequency of the ac field, h is the height of the toroidal sample, and c is the outer and b the inner diameter of the toroidal sample. Z_{sm} can be calibrated to zero, while Z_m is equal to $R_m + jX_m$, where R_m is the resistance and X_m is the reactance of the sample. This identity is used to rewrite eq 1 as eqs 2 and 3 with Z_{sm} set to zero.

$$\mu_r = \left(1 + \frac{X_m}{f\mu_0 h \ln\frac{c}{b}}\right) - j\frac{R_m}{f\mu_0 h \ln\frac{c}{b}} \qquad (2)$$

$$= \mu_r' - j\mu_r'' \qquad (3)$$

Therefore, the relative permeability can be derived from the reactance and the resistance of a one-turn inductor system. The reliability of this method was confirmed by measuring the permeability of commercially available toroidal ferrite cores such as F-23−61, F-23−67, and F-50−68. We observed that our measured values of the real part of the permeability of all the commercial toroids are consistent with the product information provided by the manufacturer, which confirms the reliability of our measurements for ac magnetic properties (Figure S10).

With this method, the relative permeability of NCs is measured as presented in Figure 4. The real part of a relative magnetic permeability is the in-phase component of the permeability,[35,85] which is defined as $\mu_r' = (B/H\mu_0) \cos \delta$, where B is the magnetic flux in the material, H is the external field intensity, μ_0 is the vacuum permeability, and δ is the phase delay of B relative to H. The magnetic flux density of a system is enhanced in proportion to the real part of the permeability. In Figure 4b, the real part of the relative permeability (μ_r') of the maghemite NCs in six different sizes shows clear size dependence. In contrast, the size dependence of μ_r' of the as-synthesized magnetite-rich NCs (Figure 4a) is not as pronounced as the maghemite NCs, reflecting the different sensitivities of the initial susceptibilities to particle size for the two sets of nanoparticle systems, as observed in the insets of Figure S8a and b. The μ_r' value of the maghemite samples increases as the NC size increases over the whole range of frequencies measured. This can be attributed to the fact that the magnetic flux density in the toroid is enhanced as the NC magnetic moment increases with increasing size of these monodomain NCs. According to the core−shell model of magnetic nanocrystals,[72] the surface-to-volume ratio decreases as the particle size increases. Assuming a shell of disordered surface spins of constant thickness,[26,86] the magnetic moment of single-domain NCs should increase with NC size,[87−89] as can be observed from the size-dependent saturation magnetization of
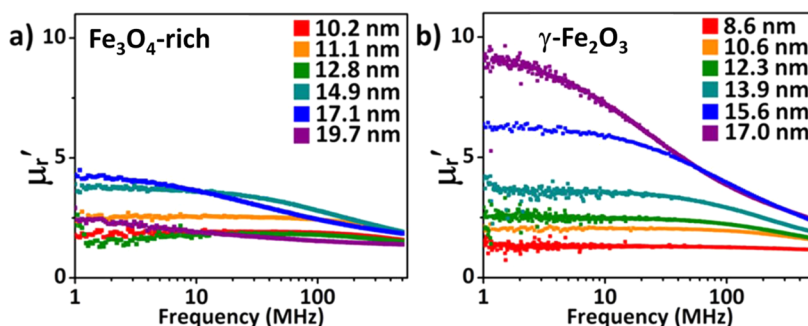
Figure 4. Real part of the relative permeability of (a) magnetite-rich iron oxide NCs and (b) maghemite iron oxide NCs.
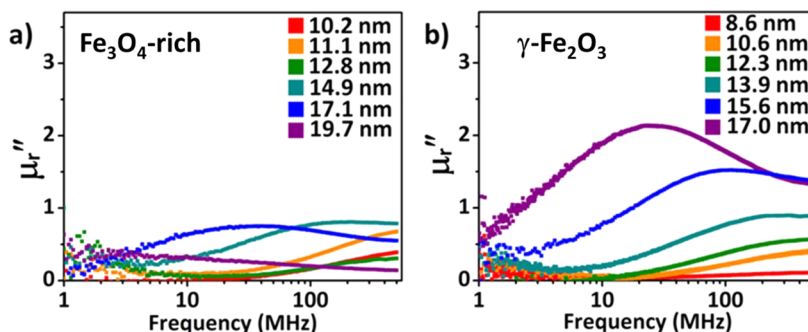

Figure 5. Imaginary part of the relative permeability of (a) magnetite-rich iron oxide NCs and (b) maghemite iron oxide NCs.

maghemite NCs in Figure S9. Still, it is notable that the μ_r' value as a function of frequency starts to drop earlier in the larger NCs. This observation is suspected to arise from the size dependence of the ferromagnetic resonance frequency.[90]

Surprisingly, the μ_r' values of the magnetite-rich NCs are smaller than those of oxidized maghemite NCs. Even though in the bulk magnetite is known for having a higher saturation magnetic moment than maghemite,[52,91] the saturation magnetization value of the magnetite-rich NC samples is similar to or smaller than that of maghemite NCs with similar size. In addition, the saturation magnetization decreases as the particle size increases (Figure S9). These observations may arise from the presence of paramagnetic wüstite and/or interfacial wüstite/magnetite phases in as-synthesized NCs, which would lower their saturation magnetization. For example, in up to 14.9 nm magnetite-rich iron oxide NCs, μ_r' values of magnetite-rich NCs are at a similar level compared to that of maghemite NCs. However, the 17.1 and 19.7 nm magnetite-rich samples do not show the real part of permeability as high as that of 15.6 and 17.0 nm. Considering the advent of the stiff slopes at around 200 K in the ZFC curves of 17.1 and 19.7 nm NCs, paramagnetic wüstite phase might start affecting the crystal structure of magnetite-rich iron oxide NCs and lower the permeability. Alternatively, the presence of a thicker spin-disordered shell on the surface of magnetite-rich particles, often referred to as a magnetic "dead layer",[92] compared to maghemite NCs will also have a similar effect of lowering the magnetization, possibly below that for the

maghemite NCs, as previously observed.[93] In addition, stronger interparticle interactions of an antiferromagnetic nature could also reduce the saturation magnetization. All these effects may contribute to the experimental observation that the size effect is not clearly expressed in as-synthesized iron oxide NCs (Figure 4a).

We consider now the measurement data of the imaginary part of the relative permeability (μ_r''). The imaginary part of permeability is the out-of-phase component of relative permeability, which is defined as $\mu_r'' = (B/H\mu_0) \sin \delta$.[94] This value is critical for low-energy-loss applications because energy loss is proportional to μ_r''. The imaginary part of the permeability of magnetite-rich (a) and maghemite (b) iron oxide NCs is presented in Figure 5. As expected, the results show a maximum that is size dependent, with the size sensitivity being much more pronounced for the maghemite samples. In Figure 5b we observe the largest size maghemite NCs to have the most pronounced maximum at a frequency of about 30 MHz, with lower maxima monotonically decreasing in magnitude and displaced to higher frequencies as the particle size decreases. In contrast, magnetite-rich NCs exhibit depressed maxima, not monotonically decreasing with size. These differences may be traced to the single-particle magnetic anisotropies and the collective behavior of the NC assemblies and the way they affect their complex ac permeability, as discussed in the SI. It should be noted that μ_r'' of maghemite nanocrystals is larger than that of magnetite-rich nanocrystals. This is because μ_r'' is proportional to μ_r', as can be seen from the following
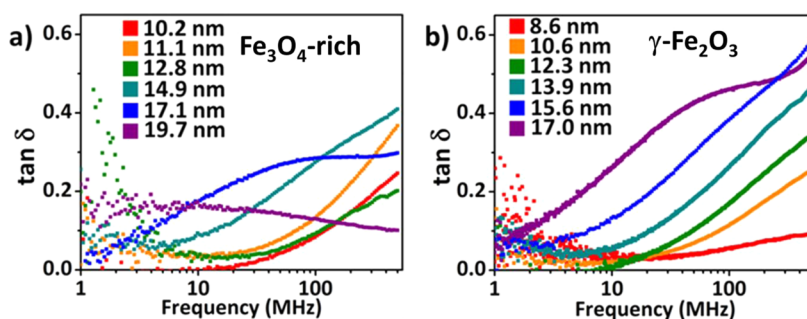
Figure 6. Loss tangent of (a) magnetite-rich iron oxide NCs and (b) maghemite iron oxide NCs.

equation: $\mu_r'' = (B/H\mu_0) \sin \delta = \mu_r' \tan \delta$. Therefore, with the similar value of the phase delay, the imaginary part of the permeability is higher in the case with the higher value of the real part of the permeability.

Energy efficiency is expressed in terms of the loss tangent, $\tan \delta$, which is the ratio between the imaginary and the real part of the permeability.[35] Materials characterized with low loss tangent are more energy efficient; they display a small phase delay between B and H. Here again, size dependence is not observed in the set of the magnetite-rich iron oxide NCs (Figure 6a), while it is clear in the case of the maghemite iron oxide NCs (Figure 6b). In the case of maghemite nanocrystals, it is quite intriguing that the points where the loss tangent starts increasing significantly vary with the size of the NCs. This suggests that optimized magnetic materials for various kinds of electronic device applications, at different operating frequencies, can be designed by tuning the size, shape, and chemical composition of magnetic NCs. For example, even though the 13.9 nm maghemite iron oxide NCs have a higher μ_r' than the 12.3 nm NCs over the whole range of the measured frequencies, it might be more energetically efficient to use 12.3 nm NCs as the inductor core for devices operating at above 10 MHz, as the loss tangent of the 13.9 nm particles is much higher than that of the 12.3 nm particles at 10 MHz. Therefore, the systems with magnetic materials working in different frequencies can perform in an optimized condition by selecting NCs with the best performance at a particular operating frequency or over a specific range of frequencies. These results support the notion that magnetic NCs are promising candidates for low-energy-loss applications through precise control in the size, shape, and chemical compositions of NCs.

The composition dependence of the magnetic permeability of our NCs is further supported by the direct comparison of as-synthesized iron oxide NCs before and after the oxidation process at high temperature, as a comparison of the permeability properties of the sample before and after aeration indicates. As-synthesized iron oxide NCs 18.3 nm in diameter are aerated at 250 °C for 2 h following the literature.[95,96] The Mössbauer data of the aerated samples indicate that wüstite is oxidized; that is, the $Fe_{1-x}O$ or interfacial

$Fe_{1-x}O/Fe_3O_4$ portion of the as-synthesized NCs is removed from the original NC structure (Figure S11 and Table S1). TEM images (Figure S12) show that there is no significant change in either the morphology or the size of NCs after the oxidation process. The superimposed SAXS curves of two samples also support that there is no change in size before and after the heating process (Figure S13). Direct comparison reveals that the coercivity at 15 K is reduced after aeration from ~216 mT to ~27 mT, which is a dramatic change (Figure S14). At 300 K, the hysteresis curves show that iron oxide NCs are saturated much faster after oxidation. Before the aeration process, as-synthesized iron oxide NCs reach 50% of their maximum magnetization at around 275 mT, while the aerated iron oxide NCs are excited 50% at around 18 mT. Consequently, as shown in Figure S15, μ_r' of iron oxide NCs becomes more than 5 times larger at 1 MHz after oxidation even though the value spontaneously decreases from 11 at 1 MHz to 4 at 500 MHz. The Mössbauer data indicate that the stoichiometry of the NCs after aeration is more related to magnetite than to maghemite without wüstite phase, thus supporting our previous discussion that the inhomogeneous crystal structure of larger as-synthesized NCs due to paramagnetic wüstite phase leads to the lower magnetic permeability of as-synthesized iron oxide NCs than aged maghemite iron oxide NCs. However, why the aerated sample shows less coercivity than aged maghemite iron oxide NCs is an observation not fully understood and still under investigation.

In order to examine the potential of using iron oxide NCs as the magnetic core of a toroidal inductor, the maghemite NCs are further processed to form a toroidal shape as shown in Figure 7. In previous reports, various kinds of polymers are used to prevent the oxidation of nanoparticles, to fix nanoparticles in a membrane, and to increase the resistance of the core.[97−102] However, the addition of polymer composites in the matrix can lower the real part of the permeability and the filling factor of the nanoparticles, which is not desirable for an inductor core. In our study, ligand exchange is adopted to make magnetic NC inductor cores. Ligand exchange with nitrosonium tetrafluoroborate is conducted to remove the organic ligand layer and replace it with inorganic
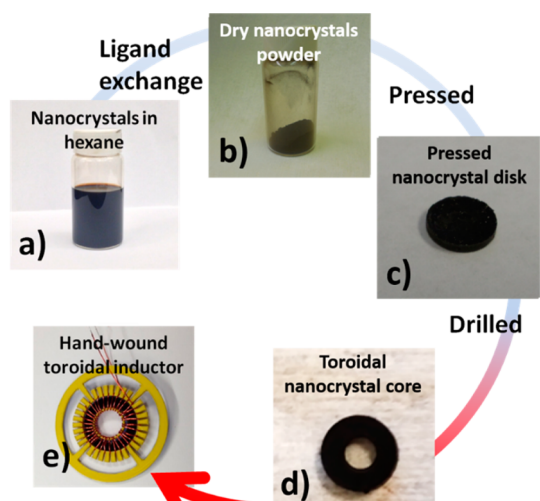
Figure 7. Steps to make hand-wound toroidal inductors with iron oxide NC cores. (a) NCs are dispersed in hexane. (b) NCs are ligand exchanged with $NOBF_4^-$ and dried under vacuum overnight to achieve an NC powder. (c) Nanoparticle powder is pressed into a disk. (d) The center of the disk is drilled to make a toroidal core. (e) The toroidal NC core is wound with a copper wire coated with polyurethane-coated nylon.

BF_4^- anions.[103] After ligand exchange, the NCs in dimethylformamide are precipitated by adding acetone and then dried under vacuum. After several hours, dry NC powder is obtained, and this powder is ground by a mortar and pestle to get a fine powder.

The fine powder is transferred into a cylindrical mold (a cylinder diameter of 6.3 mm) and pressed into a thin disk (bench top hydraulic press, Carver, Inc.) with a pressure of 70 MPa. The disk is then dip-coated with SU-8 polymer to enhance the physical stability followed by drilling a center hole of approximately 3 mm. Note that the SU-8 does not include any solvent or photoinitiator and is initially in the form of a pellet, which is subsequently melted on a hot plate at 100 °C for the dip-coating process. The dip-coated SU-8 layer is then removed with acetone so a magnetic NC toroidal core is obtained. The winding process for the toroid inductor is then begun. The toroidal core is first integrated with a laser-cut plastic bobbin to guide the winding path, and a magnet wire is uniformly hand-wound. Two different nanocrystal sizes of maghemite powders (a particle size of 13.9 and 17.0 nm) have been fabricated as toroidal inductors using the described process. The dimensions of each NC core inductor are summarized in Table 3. The toroidal inductors are electrically characterized in terms of inductance, resistance, and quality factor as a function of frequency as shown in Figure 8.

A stable inductance of approximately 300 nH for a 13.9 nm powder inductor is observed over the frequency range of 0.1 to 100 MHz, whereas the inductance of the 17.0 nm powder inductor decreased from approximately 750 nH at 0.1 MHz to 500 nH at 40 MHz, as shown in Figure 8a. The ac resistances and quality

TABLE 3. Dimensions of Iron Oxide NC Cores

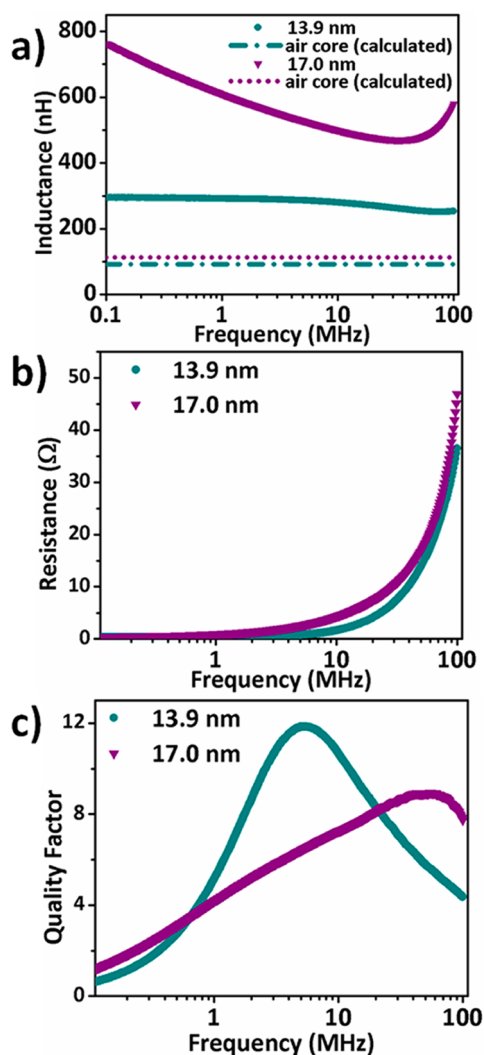|	13.9 nm γ-Fe$_2$O$_3$ nanocrystal core	17.0 nm γ-Fe$_2$O$_3$ nanocrystal core
outer diameter	6.5 mm	6.5 mm
inner diameter	3.5 mm	2 mm
thickness	680 mm	1200 mm
calculated inductance of air-core inductor	91.7 nH	113.2 nH

Figure 8. (a) Inductance, (b) resistance, and (c) quality factor of 13.9 nm (cyan) and 17.0 nm (purple) maghemite iron oxide NC cores. The frequency range is from 100 kHz to 100 MHz. The dotted lines in (a) represent the calculated inductance of the air-core inductor.

factors over the same frequency range are also shown in Figure 8b and c. The 13.9 nm inductor and the 17.0 nm inductor show resistances at 10 MHz of approximately 1.5 and 4 Ω and quality factors of 12 at 4.5 MHz and 9 at 40 MHz, respectively. As can be expected from the trend in the relative permeability data, the inductor with the 17.0 nm iron oxide NC core enhances inductance more than the inductor with a 13.9 nm iron oxide NC core because the inductance is

proportional to the real part of the permeability of the magnetic core. Even though the inductance of the 17.0 nm sample decreases from 100 kHz to 35 MHz, the inductance of the 13.9 nm sample is stable over the whole range of frequencies (100 kHz to 100 MHz). The counterpart, the resistance of the inductor, increases in both cases, with a significant increase at 10 MHz for the 13.9 nm iron oxide NC core. In the case of the quality factor, the inductors hit their peak at 5.2 MHz for the 13.9 nm iron oxide with 11.9 and at 54.6 MHz for the 17.0 nm iron oxide with 8.95. It is notable that they do not show exactly the same pattern as the quality factor measured through the one-turn inductor model. This inconsistency in the quality factor trend from the data taken by the one-turn inductor model can be attributed to the effect of ligand exchange and the resonance of the inductor itself. Ligand exchange shrinks interparticle distances.[103] Reduced interparticle distance increases magnetic coupling between nanocrystals and can produce different ac magnetic behavior from NCs with organic ligand shells. Also, the inductance and resistance were taken from the whole system, not just the core, so that the trend of the curve can deviate from the curve calculated by the one-turn inductor model. Since the data are already corrected for the impedance of the inductor without a core (Z_{sm}) eq 1, the data curve might not exactly match with the data from the hand-wound inductor. The data presented in Figure 8 show that magnetic NCs can be used as inductor cores successfully without any help from another matrix to hold the NCs together. These inductor trials indicate that there is a high potential to develop low-energy-loss materials by controlling the size and composition of NCs.

CONCLUSION

In summary, we have characterized the ac magnetic properties of iron oxide NCs at radio frequencies from 1 to 500 MHz. The compositions of as-synthesized and naturally oxidized iron oxide NCs are investigated by Mössbauer spectroscopy. The composition analysis confirms that as-synthesized iron oxide NCs are magnetite-rich and aged NCs are maghemite. In addition, a wüstite phase is also observed in the large as-synthesized iron oxide NCs. At room temperature ZFC curves and hysteresis curves show superparamagnetic behavior for both sets of iron oxide NCs. From the ZFC curves, the presence of magnetite and wüstite phase in the as-synthesized NCs is observed again. The measurements for the magnetic permeability show a clear size dependence in the maghemite NCs, but not in the magnetite-rich NCs. In maghemite iron oxide NCs, the real part of the permeability increases proportionally to the size of the NCs because the magnetic moment of single-domain NCs is in proportion to the size. On the other hand, as-synthesized iron oxide NCs did not show size-dependent magnetic permeability. This can be attributed to the inhomogeneous crystal structure of the as-synthesized NCs, which is observed from Mössbauer spectroscopy and SQUID measurements, making their magnetization smaller than what would be expected from a homogeneous magnetite phase. The aeration of the as-synthesized iron oxide NCs supports this argument. As-synthesized iron oxide NCs show no change in their morphology and size after heating at 250 °C for 2 h. However, the paramagnetic wüstite phase disappears after the heating process according to the Mössbauer data analysis, and their dc and ac magnetic properties are changed significantly. In particular, the real part of the permeability is increased dramatically to a similar value of maghemite iron oxide NCs after heating, which supports our hypothesis. Finally, inductors with maghemite iron oxide NC cores are prepared to evaluate the feasibility of inductors with magnetic NC cores. Maghemite iron oxide NCs of 13.9 and 17.0 nm are prepared in powder form, and toroidal cores were prepared to be integrated into hand-wound inductors. The measurements on the inductors show clear nanocrystal-size dependence as presented in the permeability measurements. Even though the value of the real part of the permeability is not at the same level as other traditional ferromagnetic materials such as Permalloy and Supermalloy, further investigation on low-energy-loss magnetic NCs should continue to improve the energy efficiency of magnetic components at radio frequencies in power electronic devices.

EXPERIMENTAL METHODS

Materials. All chemicals are used as purchased without any further purification. Iron(III) chloride hexahydrate (97%), oleic acid (technical grade, 70%), 1-octadecene (technical grade, 90%), and iron oxide powder (<5 μm, 98%) are purchased from Sigma-Aldrich. Sodium oleate (>97.0%) is purchased from TCI America. Commercial ferrite toroidal cores are purchased from Amidon. Magnet wire (part no. 8055) is purchased from Belden.

Synthesis of Iron Oxide Nanocrystals and Purification. Monodisperse iron oxide nanocrystals are synthesized by modifying the method reported by Hyeon et al.[46] and Chen et al.[51] First, iron oleate precursors are prepared as follows: 10.8 g of iron(III) chloride, 36.5 g of sodium oleate, 40 mL of DI water, 40 mL of

ethanol, and 80 mL of hexane are mixed into a 500 mL three-neck flask. The mixture is refluxed at 60 °C for 4 h. The red-black-colored iron oleate precursors are washed with DI water three times and dried by using a rotary evaporator. Then, the precursors are kept under vacuum overnight. Second, the 10.2 nm iron oxide nanocrystals are synthesized by adding 7.2 g of iron oleate precursors, 1 mL of oleic acid, and 20 mL of 1-octadecene into a three-neck flask. The reaction mixture is heated to 100 °C and kept under vacuum for 1 h. Then, the mixture is heated to 315 °C at a rate of 3 °C/min. After 30 min, the reaction mixture is cooled to room temperature and precipitated by adding ethanol. The precipitate is redispersed in hexane and washed with ethanol twice more. Finally, the iron oxide nanocrystals are redispersed in hexane and kept in a glovebox. By increasing the

amount of oleic acid added into the mixture, the size of the iron oxide nanocrystals is increased. Aged NCs are kept in ambient conditions over a year.

Oxidation of As-Synthesized Iron Oxide Nanocrystals. As-synthesized iron oxide nanocrystals after purification are dissolved into a mixture of 20 mL of 1-octadecene and 1 mL of oleic acid. Then, the solution is heated to 250 °C. After 2 h, the solution is cooled to room temperature and repurified by adding ethanol and centrifugation. The final product is redispersed in hexane and kept in a glovebox.

Mössbauer Spectroscopy. Mössbauer measurements were performed by using a transmission Mössbauer spectrometer. A 30 mCi ^{57}Co radioactive source was used and maintained at RT. The source was mounted on an SEE Co. (Medina, MN, USA) electromechanical drive, operated at constant acceleration. The samples were dispersed in BN and mounted into a Janis Research cryogenic dewar. Sample temperatures $4.2 < T < 300$ K were maintained by using a SEE Co. temperature controller. Spectra were fit to a superposition of iron subsites assuming Lorentzian absorption lines and allowing for distributions of hyperfine fields using the WMOSS software package, also by SEE Co.

Direct Current Magnetization Measurements. Direct current magnetic characterizations are performed by using a SQUID magnetometer with reciprocating sample option (Quantum Design MPMS-XL 7T). For the zero field cooled curves, the samples are cooled to 15 K first without an external field. Then, the magnetization of the samples is taken under an applied field of 0.01 T from 15 to 300 K. For the field-cooled curves, the samples are cooled to 15 K in the presence of a 0.01 T magnetic field first, and then the magnetization is measured under an applied field of 0.01 T from 15 to 300 K. The magnetization hysteresis curves are taken from 3 to −3 T at 300 and 15 K.

Alternating Current Characterization. Relative magnetic permeability of iron oxide nanocrystals is measured by using a 4395A Agilent network anaylzer and 16454A Agilent magnetic material test fixture. Iron oxide nanocrystals are dispersed in a mixture of hexane and octane (2:8) and deposited into a toroidal-shaped sample holder (8 mm outer diameter, 3.2 mm inner diameter, 3 mm height, and 2.5 mm depth). After filling the sample holder with dry iron oxide nanocrystals, the sample is placed into the test fixture. The sweep frequency is set to 1−500 MHz in log frequency. The reactance and resistance of the test fixture with the sample holder are measured and converted into the real and imaginary parts of the permeability by using eqs 2 and 3. The inductance and resistance of the inductor with an iron oxide nanocrystal core are collected using the 43961A RF impedance test kit. After connecting the test kit to the 4395A Agilent network analyzer, the hand-wound iron oxide core inductor is connected to the impedance test kit and the inductance and resistance are collected. The sweep frequency is set to 0.1 to 100 MHz.

Morphological and Structural Characterization. TEM images are collected using a JEM-1400 microscope and JEOL-2100 microscope at the Singh Center for Nanotechnology at the University of Pennsylvania. Wide-angle X-ray scattering data are collected using a Rigaku Smartlab high-resolution diffractometer with Cu Kα radiation (λ = 1.5416 Å). Small-angle X-ray scattering data are taken at the Multi-Angle X-ray Scattering Facility at the University of Pennsylvania. Small-angle X-ray scattering data are analyzed using Datasqueeze software.

Conflict of Interest: The authors declare no competing financial interest.

Supporting Information Available: Details regarding the histograms of the size measurement from TEM images, WAXS data, full ZFC-FC curves, full sweep 300 K and 15 K magnetic hysteresis curves, frequency dependence of the real and imaginary parts of the magnetic susceptibility, magnetic permeability measurements for reference toroids, Mössbauer spectroscopy, SAXS, and dc and ac magnetic characterization data for iron oxide nanocrystals before and after the aeration process. This material is available free of charge *via* the Internet at http://pubs.acs.org.

REFERENCES AND NOTES

1. Desvaux, C.; Amiens, C.; Fejes, P.; Renaud, P.; Respaud, M.; Lecante, P.; Snoeck, E.; Chaudret, B. Multimillimetre-Large Superlattices of Air-Stable Iron-Cobalt Nanoparticles. *Nat. Mater.* **2005**, *4*, 750–753.
2. Desvaux, C.; Dumestre, F.; Amiens, C.; Respaud, M.; Lecante, P.; Snoeck, E.; Fejes, P.; Renaud, P.; Chaudret, B. Face Nanoparticles from an Organometallic Approach: Synthesis, Organisation and Physical Properties. *J. Mater. Chem.* **2009**, *19*, 3268.
3. Sun, S.; Murray, C. B.; Weller, D.; Folks, L.; Moser, A. Monodisperse FePt Nanoparticles and Ferromagnetic FePt Nanocrystal Superlattices. *Science* **2000**, *287*, 1989–1992.
4. Brosseau, C.; Talbot, P. Effective Magnetic Permeability of Ni and Co Micro- and Nanoparticles Embedded in a ZnO Matrix. *J. Appl. Phys.* **2005**, *97*, 104325.
5. Song, N.-N.; Yang, H.-T.; Liu, H.-L.; Ren, X.; Ding, H.-F.; Zhang, X.-Q.; Cheng, Z.-H. Exceeding Natural Resonance Frequency Limit of Monodisperse Fe$_3$O$_4$ Nanoparticles *via* Superparamagnetic Relaxation. *Sci. Rep.* **2013**, *3*, 3161.
6. Kura, H.; Ogawa, T.; Tate, R.; Hata, K.; Takahashi, M. Size Effect of Fe Nanoparticles on the High-Frequency Dynamics of Highly Dense Self-Organized Assemblies. *J. Appl. Phys.* **2012**, *111*, 07B517.
7. Paik, T.; Gordon, T. R.; Prantner, A. M.; Yun, H.; Murray, C. B. Designing Tripodal and Triangular Gadolinium Oxide Nanoplates and Self-Assembled Nanofibrils as Potential Multimodal Bioimaging Probes. *ACS Nano* **2013**, 2850–2859.
8. Kim, B. H.; Lee, N.; Kim, H.; An, K.; Park, Y. I.; Choi, Y.; Shin, K.; Lee, Y.; Kwon, S. G.; Na, H. B.; *et al*. Large-Scale Synthesis of Uniform and Extremely Small-Sized Iron Oxide Nanoparticles for High-Resolution T_1 Magnetic Resonance Imaging Contrast Agents. *J. Am. Chem. Soc.* **2011**, *133*, 12624–12631.
9. Tromsdorf, U. I.; Bigall, N. C.; Kaul, M. G.; Bruns, O. T.; Nikolic, M. S.; Mollwitz, B.; Sperling, R. A.; Reimer, R.; Hohenberg, H.; Parak, W. J.; *et al*. Size and Surface Effects on the MRI Relaxivity of Manganese Ferrite Nanoparticle Contrast Agents. *Nano Lett.* **2007**, *7*, 2422–2427.
10. Issadore, D.; Chung, J.; Shao, H.; Liong, M.; Ghazani, A. A.; Castro, C. M.; Weissleder, R.; Lee, H. Ultrasensitive Clinical Enumeration of Rare Cells *ex Vivo* Using a Micro-Hall Detector. *Sci. Transl. Med.* **2012**, *4*, 141–192.
11. Fortin, J.-P.; Wilhelm, C.; Servais, J.; Ménager, C.; Bacri, J.-C.; Gazeau, F. Size-Sorted Anionic Iron Oxide Nanomagnets as Colloidal Mediators for Magnetic Hyperthermia. *J. Am. Chem. Soc.* **2007**, *129*, 2628–2635.
12. Lee, J.-H.; Jang, J.-T.; Choi, J.-S.; Moon, S. H.; Noh, S.-H.; Kim, J.-W.; Kim, J.-G.; Kim, I.-S.; Park, K. I.; Cheon, J. Exchange-Coupled Magnetic Nanoparticles for Efficient Heat Induction. *Nat. Nanotechnol.* **2011**, *6*, 418–422.
13. Ruan, S.; Xu, B.; Suo, H.; Wu, F.; Xiang, S.; Zhao, M. Microwave Absorptive Behavior of ZnCo-Substituted W-Type Ba Hexaferrite Nanocrystalline Composite Material. *J. Magn. Magn. Mater.* **2000**, *212*, 175–177.
14. Li, Y.; Zhang, J.; Liu, Z.; Liu, M.; Lin, H.; Che, R. Morphology-Dominant Microwave Absorption Enhancement and

Electron Tomography Characterization of CoO Self-Assembly 3d Nano-Flowers. *J. Mater. Chem. C* **2014**, *2*, 5216.

15. Pan, G.; Zhu, J.; Ma, S.; Sun, G.; Yang, X. Enhancing the Electromagnetic Performance of Co through the Phase-Controlled Synthesis of Hexagonal and Cubic Co Nanocrystals Grown on Graphene. *ACS Appl. Mater. Interfaces* **2013**, *5*, 12716–12724.

16. Qiu, J.; Sullivan, C. R. Design and Fabrication of VHF Tapped Power Inductors Using Nanogranular Magnetic Films. *IEEE Trans. Power Electron.* **2012**, *27*, 4965–4975.

17. Kim, J.; Ni, W.; Lee, C.; Kan, E. C.; Hosein, I. D.; Song, Y.; Liddell, C. Magnetic Property Characterization of Magnetite (Fe_3O_4) Nanorod Cores for Integrated Solenoid rf Inductors. *J. Appl. Phys.* **2006**, *99*, 08R903.

18. Huang, W.; Yu, X.; Froeter, P.; Xu, R.; Ferreira, P.; Li, X. On-Chip Inductors with Self-Rolled-up SiN_x Nanomembrane Tubes: A Novel Design Platform for Extreme Miniaturization. *Nano Lett.* **2012**, *12*, 6283–6288.

19. Choi, C.; Yoo, H. S.; Oh, J. M. Preparation and Heat Transfer Properties of Nanoparticle-in-Transformer Oil Dispersions as Advanced Energy-Efficient Coolants. *Curr. Appl. Phys.* **2008**, *8*, 710–712.

20. Guan, W.; Jin, M.; Fan, Y.; Chen, J.; Xin, P.; Li, Y.; Dai, K.; Zhang, H.; Huang, T.; Ruan, J. Finite Element Modeling of Heat Transfer in a Nanofluid Filled Transformer. *IEEE Trans. Magn.* **2014**, *50*, 253–256.

21. Miao, J.; Dong, M.; Ren, M.; Wu, X.; Shen, L.; Wang, H. Effect of Nanoparticle Polarization on Relative Permittivity of Transformer Oil-Based Nanofluids. *J. Appl. Phys.* **2013**, *113*, 204103.

22. Bosch-Jimenez, P.; Yu, Y.; Lira-Cantu, M.; Domingo, C.; Ayllón, J. A. Solution Processable Titanium Dioxide Precursor and Nanoparticulated Ink: Application in Dye Sensitized Solar Cells. *J. Colloid Interface Sci.* **2014**, *416*, 112–118.

23. Cozzoli, P. D.; Kornowski, A.; Weller, H. Low-Temperature Synthesis of Soluble and Processable Organic-Capped Anatase TiO_2 Nanorods. *J. Am. Chem. Soc.* **2003**, *125*, 14539–14548.

24. Panthani, M. G.; Akhavan, V.; Goodfellow, B.; Schmidtke, J. P.; Dunn, L.; Dodabalapur, A.; Barbara, P. F.; Korgel, B. A. Synthesis of $CuInS_2$, $CuInSe_2$, and $Cu(In_xGa_{1-x})Se_2$ (CIGS) Nanocrystal "Inks" for Printable Photovoltaics. *J. Am. Chem. Soc.* **2008**, *2*, 16770–16777.

25. Sun, Q.; Wang, Y. A.; Li, L. S.; Wang, D.; Zhu, T.; Xu, J.; Yang, C.; Li, Y. Bright, Multicoloured Light-Emitting Diodes Based on Quantum Dots. *Nat. Photonics* **2007**, *1*, 717–722.

26. Noh, S.-H.; Na, W.; Jang, J.-T.; Lee, J.-H.; Lee, E. J.; Moon, S. H.; Lim, Y.; Shin, J.-S.; Cheon, J. Nanoscale Magnetism Control *via* Surface and Exchange Anisotropy for Optimized Ferrimagnetic Hysteresis. *Nano Lett.* **2012**, *12*, 3716–3721.

27. Sun, S.; Zeng, H.; Robinson, D. B.; Raoux, S.; Rice, P. M.; Wang, S. X.; Li, G. Monodisperse MFe_2O_4 (M = Fe, Co, Mn) Nanoparticles. *J. Am. Chem. Soc.* **2004**, *4*, 126–132.

28. Sun, S.; Murray, C. B. Synthesis of Monodisperse Cobalt Nanocrystals and Their Assembly into Magnetic Superlattices (Invited). *J. Appl. Phys.* **1999**, *85*, 4325.

29. Park, T.-J.; Papaefthymiou, G. C.; Viescas, A. J.; Moodenbaugh, A. R.; Wong, S. S. Size-Dependent Magnetic Properties of Single-Crystalline Multiferroic $BiFeO_3$ Nanoparticles. *Nano Lett.* **2007**, *7*, 766–772.

30. Araghchini, M.; Chen, J.; Doan-nguyen, V.; Harburg, D. V.; Jin, D.; Kim, J.; Kim, M. S.; Lim, S.; Lu, B.; Piedra, D.; *et al.* A Technology Overview of the Powerchip Development Program. *IEEE Trans. Power Electron.* **2013**, *28*, 4182–4201.

31. Allen, M. G. Packaging-Compatible High Q Microinductors and Microfilters for Wireless Applications. *IEEE Trans. Adv. Packag.* **1999**, *22*, 207–213.

32. Korenivski, V. GHz Magnetic Film Inductors. *J. Magn. Magn. Mater.* **2000**, *216*, 800–806.

33. Zhang, X.; Ekiert, T.; Unruh, K. M.; Xiao, J. Q.; Golt, M.; Wu, R. High Frequency Properties of Polymer Composites

Consisting of Aligned Fe Flakes. *J. Appl. Phys.* **2006**, *99*, 08M914.

34. Sullivan, C. R.; Harburg, D. V.; Qiu, J.; Levey, C. G.; Yao, D. Integrating Magnetics for On-Chip Power: A Perspective. *IEEE Trans. Power Electron.* **2013**, *28*, 4342–4353.

35. Snelling, E. C.; Giles, A. D. *Ferrites for Inductors and Transformers*; Research Studies Press/Wiley: Letchworth Herts./New York, 1983; Chapter 3.

36. Jiles, D. C.; Atherton, D. L. Theory of Ferromagentic Hysteresis. *J. Magn. Magn. Mater.* **1986**, *61*, 48–60.

37. Spaldin, N. A. *Magnetic Materials: Fundamentals and Applications*, 2nd ed.; Cambridge University Press: UK, 2011; Chapter 7.

38. Sullivan, C. R.; Sanders, S. R. Design of Microfabricated Transformers and Inductors for High-Freuquency Power Conversion. *IEEE Trans. Power Electron* **1996**, *11*, 228–238.

39. Cullity, B. D. *Introduction to Magnetic Materials*, 2nd ed.; IEEE Press/Wiley: Hoboken/Piscataway, NJ, 2009; Chapter 13.

40. Dutz, S.; Hergt, R.; Mürbe, J.; Müller, R.; Zeisberger, M.; Andrä, W.; Töpfer, J.; Bellemann, M. E. Hysteresis Losses of Magnetic Nanoparticle Powders in the Single Domain Size Range. *J. Magn. Magn. Mater.* **2007**, *308*, 305–312.

41. Brown, W. B. J. Thermal Fluctuations of a Single-Domain Particle. *Phys. Rev.* **1963**, *130*, 1677–1686.

42. Spaldin, N. A. *Magnetic Materials: Fundamentals and Applications*, 2nd ed.; Cambridge University Press: UK, 2011; Chapter 12.

43. Murray, C. B.; Sun, S.; Doyle, H.; Betley, T. Monodisperse 3d (Co, Ni, Fe) Nanoparticles and Their Assembly into Nanoparticle. *MRS Bull.* **2001**, *26*, 985–991.

44. Guardia, P.; Di Corato, R.; Lartigue, L.; Wilhelm, C.; Espinosa, A.; Garcia-Hernandez, M.; Gazeau, F.; Manna, L.; Pellegrino, T. Water-Soluble Iron Oxide Nanocubes with High Values of Specific Absorption Rate for Cancer Cell Hyperthermia Treatment. *ACS Nano* **2012**, *6*, 3080–3091.

45. Hergt, R.; Andrä, W.; Ambly, C. G.; Hilger, I.; Kaiser, W. A.; Richter, U.; Schmidt, H.-G. Physical Limits of Hyperthermia Using Magnetite Fine Particles. *IEEE Trans. Magn.* **1998**, *34*, 3745–3754.

46. Park, J.; An, K.; Hwang, Y.; Park, J.-G.; Noh, H.-J.; Kim, J.-Y.; Park, J.-H.; Hwang, N.-M.; Hyeon, T. Ultra-Large-Scale Syntheses of Monodisperse Nanocrystals. *Nat. Mater.* **2004**, *3*, 891–895.

47. Park, J.; Kang, E.; Son, S. U.; Park, H. M.; Lee, M. K.; Kim, J.; Kim, K. W.; Noh, H.-J.; Park, J.-H.; Bae, C. J.; *et al.* Monodisperse Nanoparticles of Ni and NiO: Synthesis, Characterization, Self-Assembled Superlattices, and Catalytic Applications in the Suzuki Coupling Reaction. *Adv. Mater.* **2005**, *17*, 429–434.

48. Johnston-Peck, A. C.; Wang, J.; Tracy, J. B. Synthesis and Structural and Magnetic Characterization of Ni(Core)/NiO(Shell) Nanoparticles. *ACS Nano* **2009**, *3*, 1077–1084.

49. Gilbert, B.; Katz, J. E.; Denlinger, J. D.; Yin, Y.; Falcone, R.; Waychunas, G. A. Soft X-ray Spectroscopy Study of the Electronic Structure of Oxidized and Partially Oxidized Magnetite Nanoparticles. *J. Phys. Chem. C* **2010**, *114*, 21994–22001.

50. Rebodos, R. L.; Vikesland, P. J. Effects of Oxidation on the Magnetization of Nanoparticulate Magnetite. *Langmuir* **2010**, *26*, 16745–16753.

51. Chen, J.; Ye, X.; Oh, S. J.; Kikkawa, J. M.; Kagan, C. R.; Murray, C. B. Bistable Magnetoresistance Switching in Exchange-Coupled $CoFe_2O_4-Fe_3O_4$ Binary Nanocrystal Superlattices by Self-Assembly and Thermal Annealing. *ACS Nano* **2013**, *7*, 1478–1486.

52. Roca, A. G.; Marco, J. F.; Morales, M. D. P.; Serna, C. J. Effect of Nature and Particle Size on Properties of Uniform Magnetite and Maghemite Nanoparticles. *J. Phys. Chem. C* **2007**, *111*, 18577–18584.

53. Papaefthymiou, G. C. Nanostructural Studies by Mössbauer Spectroscopy. *MRS Proc.* **1994**, *332*, 261–266.

54. Greenwood, N. N.; Gibb, T. C. *Mössbauer Spectroscopy*; Chapman and Hall: London, 1971.

55. Mørup, S.; Topsøe, H. Mössbauer Studies of Thermal Excitations in Magnetically Ordered Microcrystals. *Appl. Phys.* **1976**, *11*, 63–66.

56. Papaefthymiou, G.; Devlin, E.; Simopoulos, A.; Yi, D.; Riduan, S.; Lee, S.; Ying, J. Interparticle Interactions in Magnetic Core/Shell Nanoarchitectures. *Phys. Rev. B* **2009**, *80*, 024406.

57. Verwey, E. J. W. Electronic Conduction of Magnetite (Fe_3O_4) and Its Transition Point at Low Temperatures. *Nature* **1939**, *144*, 327–328.

58. Doriguetto, A. C.; Fernandes, N. G.; Persiano, A. I. C.; Nunes Filho, E.; Greneche, J. M.; Fabris, J. D. Characterization of a Natural Magnetite. *Phys. Chem. Miner.* **2003**, *30*, 249–255.

59. Dézsi, I.; Szucs, I.; Fetzer, C. Iron Implantation in α-Al_2O_3. *J. Appl. Phys.* **2008**, *104*, 034904.

60. Redl, F. X.; Black, C. T.; Papaefthymiou, G. C.; Sandstrom, R. L.; Yin, M.; Zeng, H.; Murray, C. B.; O'Brien, S. P. Magnetic, Electronic, and Structural Characterization of Nonstoichiometric Iron Oxides at the Nanoscale. *J. Am. Chem. Soc.* **2004**, *126*, 14583–14599.

61. McCammon, C. A.; Price, D. C. Mössbauer Spectra of Fe_xO (x > 0.95). *Phys. Chem. Miner.* **1985**, *11*, 250–254.

62. Lak, A.; Kraken, M.; Ludwig, F.; Kornowski, A.; Eberbeck, D.; Sievers, S.; Litterst, F. J.; Weller, H.; Schilling, M. Size Dependent Structural and Magnetic Properties of FeO-Fe_3O_4 Nanoparticles. *Nanoscale* **2013**, *5*, 12286–12295.

63. Gorski, C. A.; Scherer, M. M. Determination of Nanoparticulate Magnetite Stoichiometry by Mössbauer Spectroscopy, Acidic Dissolution, and Powder X-ray Diffraction: A Critical Review. *Am. Mineral.* **2010**, *95*, 1017–1026.

64. Bean, C. P.; Livingston, J. D. Superparamagnetism. *J. Appl. Phys.* **1959**, *30*, S120.

65. Nunes, W.; Folly, W.; Sinnecker, J.; Novak, M. Temperature Dependence of the Coercive Field in Single-Domain Particle Systems. *Phys. Rev. B* **2004**, *70*, 014419.

66. Makhlouf, S. A.; Parker, F. T. Magnetic Hysteresis Anomalies in Ferritin. *Phys. Rev. B* **1997**, *55*, 717–720.

67. Knobel, M.; Nunes, W. C.; Winnischofer, H.; Rocha, T. C. R.; Socolovsky, L. M.; Mayorga, C. L.; Zanchet, D. Effects of Magnetic Interparticle Coupling on the Blocking Temperature of Ferromagnetic Nanoparticle Arrays. *J. Non-Cryst. Solids* **2007**, *353*, 743–747.

68. Mørup, S.; Hansen, M. F.; Frandsen, C. Magnetic Interactions between Nanoparticles. *Beilstein J. Nanotechnol.* **2010**, *1*, 182–190.

69. Huang, D. J.; Chang, C. F.; Jeng, H.-T.; Guo, G. Y.; Lin, H.-J.; Wu, W. B.; Ku, H. C.; Fujimori, A.; Takahashi, Y.; Chen, C. T. Spin and Orbital Magnetic Moments of Fe_3O_4. *Phys. Rev. Lett.* **2004**, *93*, 077204.

70. Cullity, B. D. *Introduction to Magnetic Materials*, 2nd ed.; IEEE Press/Wiley: Hoboken/Piscataway, NJ, 2009; Chapter 7.

71. O'Handley, R. C. *Modern Magnetic Materials, Principles and Applications*; John Wiley & Son, Inc., 2000.

72. Papaefthymiou, G. C. Nanoparticle Magnetism. *Nano Today* **2009**, *4*, 438–447.

73. Bødker, F.; Mørup, S.; Linderoth, S. Surface Effects in Metallic Iron Nanoparticles. *Phys. Rev. Lett.* **1994**, *72*, 8–11.

74. Walz, F. The Verwey Transition—a Topical Review. *J. Phys.: Condens. Matter* **2002**, *285*, R285–R340.

75. Yang, J. B.; Zhou, X. D.; Yelon, W. B.; James, W. J.; Cai, Q.; Gopalakrishnan, K. V.; Malik, S. K.; Sun, X. C.; Nikles, D. E. Magnetic and Structural Studies of the Verwey Transition in $Fe_{3-δ}O_4$ Nanoparticles. *J. Appl. Phys.* **2004**, *95*, 7540.

76. Daou, T. J.; Pourroy, G.; Begin-Colin, S.; Grenèche, J. M.; Ulhaq-Bouillet, C.; Legaré, P.; Bernhardt, P.; Leuvrey, C.; Rogez, G. Hydrothermal Synthesis of Monodisperse Magnetite Nanoparticles. *Chem. Mater.* **2006**, 4399–4404.

77. Nikiforov, V. N.; Koksharov, Y. A.; Polyakov, S. N.; Malakho, A. P.; Volkov, A. V.; Moskvina, M. A.; Khomutov, G. B.; Irkhin, V. Y. Magnetism and Verwey Transition in Magnetite Nanoparticles in Thin Polymer Film. *J. Alloys Compd.* **2013**, *569*, 58–61.

78. Aragón, R. Cubic Magnetic Anisotropy of Nonstoichiometric Magnetite. *Phys. Rev. B* **1992**, *46*, 5334–5338.

79. Cullity, B. D. *Introduction to Magnetic Materials*, 2nd ed.; IEEE Press/Wiley: Hoboken/Piscataway, NJ, 2009; Chapter 9.

80. Goya, G. F.; Berquó, T. S.; Fonseca, F. C.; Morales, M. P. Static and Dynamic Magnetic Properties of Spherical Magnetite Nanoparticles. *J. Appl. Phys.* **2003**, *94*, 3520.

81. Hadjipanayis, G. C.; Sellmyer, D. J.; Brandt, B. L. Rare-Earth-Rich Metallic Glasses. I. Magnetic Hysteresis. *Phys. Rev. B* **1981**, *23*, 3349–3354.

82. Lucchini, M. A.; Riani, P.; Canepa, F. Quantitative Analysis of the A.C. Susceptibility of Core−Shell Nanoparticles. *J. Nanopart. Res.* **2013**, 15.

83. Shenhui, J.; Quanxing, J. An Alternative Method to Determine the Initial Permeability of Ferrite Core Using Network Analyzer. *IEEE Trans. Electromagn. Compat.* **2005**, *47*, 651–657.

84. *Agilent 16454 Magnetic Material Fixture Operation and Service Manual*; Agilent, 2001.

85. Spaldin, N. A. *Magnetic Materials: Fundamentals and Applications*, 2nd ed.; Cambridge University Press: UK, 2011; Chapter 2.

86. Tronc, E.; Ezzir, A.; Cherkaoui, R.; Chane, C.; Kachkachi, H.; Fiorani, D.; Testa, A. M.; Grene, J. M.; Jolivet, J. P. Surface-Related Properties of γ-Fe_2O_3 Nanoparticles. *J. Magn. Magn. Mater.* **2000**, *221*, 63–79.

87. Iida, H.; Takayanagi, K.; Nakanishi, T.; Osaka, T. Synthesis of Fe_3O_4 Nanoparticles with Various Sizes and Magnetic Properties by Controlled Hydrolysis. *J. Colloid Interface Sci.* **2007**, *314*, 274–280.

88. Huang, C.-C.; Chuang, K.-Y.; Chou, C.-P.; Wu, M.-T.; Sheu, H.-S.; Shieh, D.-B.; Tsai, C.-Y.; Su, C.-H.; Lei, H.-Y.; Yeh, C.-S. Size-Control Synthesis of Structure Deficient Truncated Octahedral $Fe_{3-δ}O_4$ Nanoparticles: High Magnetization Magnetites as Effective Hepatic Contrast Agents. *J. Mater. Chem.* **2011**, *21*, 7472.

89. Demortière, A.; Panissod, P.; Pichon, B. P.; Pourroy, G.; Guillon, D.; Donnio, B.; Bégin-Colin, S. Size-Dependent Properties of Magnetic Iron Oxide Nanocrystals. *Nanoscale* **2011**, *3*, 225–232.

90. Diehl, M. R.; Yu, J.-Y.; Heath, J. R.; Held, G. A.; Doyle, H.; Sun, S.; Murray, C. B. Crystalline, Shape, and Surface Anisotropy in Two Crystal Morphologies of Superparamagnetic Cobalt Nanoparticles by Ferromagnetic Resonance. *J. Phys. Chem. B* **2001**, *105*, 7913–7919.

91. Cullity, B. D. *Introduction to Magnetic Materials*, 2nd ed.; IEEE Press/Wiley: Hoboken/Piscataway, NJ, 2009; Chapter 6.

92. Sato, T.; Iiljima, T.; Seki, M.; Inagaki, N. Magnetic Properties of Ultrafine Ferrite Particles. *J. Magn. Magn. Mater.* **1987**, *65*, 252–256.

93. Burnham, P.; Dollahon, N.; Li, C. H.; Viescas, A. J.; Papaefthymiou, G. C. Magnetization and Specific Absorption Rate Studies of Ball-Milled Iron Oxide Nanoparticles for Biomedicine. *J. Nanopart.* **2013**, *2013*, 1–13.

94. Cullity, B. D. *Introduction to Magnetic Materials*, 2nd ed.; IEEE Press/Wiley: Hoboken/Piscataway, NJ, 2009; Chapter 12.

95. Sun, S.; Zeng, H. Size-Controlled Synthesis of Magnetite Nanoparticles. *J. Am. Chem. Soc.* **2002**, 8204–8205.

96. Woo, K.; Hong, J.; Choi, S.; Lee, H.-W.; Ahn, J.-P.; Kim, C. S.; Lee, S. W. Easy Synthesis and Magnetic Properties of Iron Oxide Nanoparticles. *Chem. Mater.* **2004**, 2814–2818.

97. Riahi-Kashani, M. E.-R. A. Permeability Evaluation of Ferrite Pastes, Epoxies, and Substrates over a Wide Range of Frequencies. *IEEE Trans. Instrum. Meas.* **1992**, *41*, 1036–1040.

98. Markondeya Raj, P.; Sharma, H.; Samtani, S.; Mishra, D.; Nair, V.; Tummala, R. Magnetic Losses in Metal Nanoparticle-Insulator Nanocomposites. *J. Mater. Sci. - Mater. Electron.* **2013**, *24*, 3448–3455.

99. Raj, P. M.; Sharma, H.; Reddy, G. P.; Reid, D.; Altunyurt, N.; Swaminathan, M.; Tummala, R.; Nair, V. Novel Nanomagnetic Materials for High-Frequency RF Applications.

In *IEEE Electronic Components and Technology Conference (ECTC)*; IEEE, **2011**; pp 1244−1249.

100. Bedair, S. S.; Meyer, C. D.; Morgan, B. Closed Core Inductor and High-K Dielectric Capacitor Fabrication through Evaporation Driven Nanoparticle Assembly in Capillaries. *J. Appl. Phys.* **2011**, *109*, 07E702.

101. Wong, C. P.; Zhang, Z. J. Magnetic Nanocomposite for High Q Embedded Inductor. In *IEEE Consumer Communications and Networking Conference*; IEEE, **2004**; pp 171−174.

102. Yang, C.; Koh, K.; Zhu, X.; Lin, L. On-Chip RF Inductors with Magnetic Nano Particles Medium. *Solid-State Sensors, Actuators and Microsystems Conference (TRANSDUCERS)*; **2011; pp** , 2801−2804.

103. Dong, A.; Ye, X.; Chen, J.; Kang, Y.; Gordon, T.; Kikkawa, J. M.; Murray, C. B. A Generalized Ligand-Exchange Strategy Enabling Sequential Surface Functionalization of Colloidal Nanocrystals. *J. Am. Chem. Soc.* **2011**, *133*, 998−1006.